Appl Nanosci (2016) 6:1199–1210
DOI 10.1007/s13204-016-0531-1

ORIGINAL ARTICLE

The effect of post annealing treatment on the citrate sol–gel derived nanocrystalline $BaFe_{12}O_{19}$ powder: structural, morphological, optical and magnetic properties

B. C. Brightlin[1] · **S. Balamurugan**[1]

Received: 30 March 2016 / Accepted: 25 April 2016 / Published online: 6 May 2016

Abstract The nanocrystalline $BaFe_{12}O_{19}$ powders were obtained from citrate sol–gel combustion-derived powder upon annealing at 800–1100 °C, and explored their structural, micro-structural, optical and magnetic properties. The thermal decomposition of citrate sol–gel combustion product was verified by means of thermogravimetric and differential thermal analysis. Structural identification of the citrate sol–gel combustion powder and annealed samples were investigated by powder X-ray diffraction. Though the combustion product exhibits cubic spinel phase material, the annealed powder yields good quality nanocrystalline hexagonal $BaFe_{12}O_{19}$ phase materials. The thin plate-like flakes morphology with random particle sizes of ~100–200 nm with slightly agglomerated particles of $BaFe_{12}O_{19}$ phase is analyzed by high resolution scanning electron microscopy for the good quality annealed sample. Photoluminescence emission spectrum of $BaFe_{12}O_{19}$ material reveals broad emission peak at ~360 nm under the excitation wavelength of 270 nm. Interestingly, the near infrared relative reflectivity of the nanocrystalline $BaFe_{12}O_{19}$ materials obtained by citrate sol-gel synthesis method is higher than the nanocrystalline $BaFe_{12}O_{19}$ materials obtained by mechano-thermal and co-precipitation method. The present dark brown colored $BaFe_{12}O_{19}$ materials can be applied as a ceramic color pigment which includes several applications. The room temperature magnetic hysteresis loop of the annealed $BaFe_{12}O_{19}$ sample exhibits a ferromagnetic saturation magnetization, M_s of 55.774 emu/g at 15 kOe.

Keywords Hexa-ferrite · $BaFe_{12}O_{19}$ · Citrate sol–gel combustion · Annealing · Optical properties · Morphology

Introduction

Barium hexa-ferrite, $BaFe_{12}O_{19}$ is a permanent magnetic material which has extensively used in many interesting magnetic device applications (Durmus et al. 2011; Jiang et al. 2010; Shang et al. 2007; Vinod et al. 2011) due to its high chemical stability, corrosion resistivity, low cost, high resistivity, superior and anti-erosion properties and mechanical hardness. For the application of the material in different fields, the material has to be synthesized in pure form, and subsequently well characterized by different techniques. For example, different preparation techniques, such as solid state reaction (Qiu et al. 2005), mechano-thermal (Balamurugan et al. 2015), molten salt method (Topal et al. 2007), co-precipitation method (Radwan et al. 2007), citrate sol–gel (Mali and Ataie 2005), hydrothermal method (Wang et al. 2004) and reverse micelle technique (Xu et al. 2008) have been followed to design and develop the micro and nanoscale $BaFe_{12}O_{19}$ materials. Among these different methods, we have selected citrate sol–gel method as it has many advantages which include relatively simple, cost effective and independence of the processing parameters, etc. (Mali and Ataie 2005). Hitherto there have been several investigations reported for the citrate sol–gel processed $BaFe_{12}O_{19}$ materials (Durmus et al. 2011; Mali and Ataie 2005; Birsoza et al. 2010; Xu et al. 2006; Sozeri et al. 2012; Jiang and Ai 2010; Mali and Ataie 2004; Qiu and Gu 2006). To obtain the $BaFe_{12}O_{19}$ materials, different

---

✉ S. Balamurugan
scandium.chemistry@gmail.com

[1] Advanced Nanomaterials Research Laboratory, Department of Nanotechnology, Noorul Islam Centre for Higher Education, Kumaracoil, Thuckalay 629 180, Tamilnadu, India

molar ratio of Ba:Fe:citricacid have been adopted (Durmus et al. 2011; Jiang et al. 2010; Xu et al. 2006; Mali and Ataie 2004; Chen et al. 2012; Ting and Wu 2010; Mali and Ataie 2005). According to the previous reports, the sol–gel processed materials are characterized by X-ray diffraction (Murthy et al. 2012; Liu and Xiang 2010; Song et al. 2010; Ping et al. 2008; Ebrahimi et al. 2012), thermal gravimetric analysis (Yu and Huang 2003; Yu and Liu 2006), Fourier-transform infrared, scanning electron microscope (Liu and Xiang 2010; Song et al. 2010; Ebrahimi et al. 2012), transmission electron microscope (Murthy et al. 2012), magnetometer (Durmus et al. 2011; Mali and Ataie 2005; Birsoza et al. 2010; Xu et al. 2006; Sozeri et al. 2012; Jiang and Ai 2010; Mali and Ataie 2004; Qiu and Gu 2006) for quality, phase formation, thermal decomposition, surface morphology, and magnetic property of the synthesized $BaFe_{12}O_{19}$ materials. From our recent near infrared (NIR) reflectivity study (Balamurugan et al. 2015), the $BaFe_{12}O_{19}$ material obtained by mechano-thermal process has been identified as NIR reflective color pigment due to its high NIR reflectivity in the region of wavelength 1750–2000 nm. Subsequent to our recent study, in the present work we have explored the detailed studies on the synthesis and characterization of citrate sol–gel derived $BaFe_{12}O_{19}$ materials by powder XRD, TG–DTA, FT-IR, NIR, PL, HRSEM-EDX, and vibrating sample magnetometer.

Experimental

Materials preparation

The nanocrystalline $BaFe_{12}O_{19}$ powders were prepared by citrate sol–gel auto combustion method using $Ba(NO_3)_2$, $Fe(NO_3)_3.9H_2O$ and citric acid as precursors in the molar ratio of 1:12:13. The appropriate amount of commercially available $Ba(NO_3)_2$ (1 g) and $Fe(NO_3)_3.9H_2O$ (18.5436 g) were first dissolved in minimum quantity (20 ml) of deionized water in separate borosil glass beaker. The pH of the solutions of $Ba(NO_3)_2$ and $Fe(NO_3)_3.9H_2O$ were 6 and 1, respectively. Then, 10.4531 g of citric acid was dissolved in deionized water and its pH value noted as 2. Then, both nitrate solutions were mixed together and stirred well using a magnetic stirrer at 300 rpm for 15 min. After mixing, the citric acid solution was added dropwise in the nitrate solution and stirred well for 30 min which resulted in a deep red solution with a pH value of 2. The ammonia solution was added dropwise to the above solution to adjust the pH value to 7. The resulting solution was stirred for 30 min at ~75 °C in a magnetic stirrer and continued the heating in a heating mantle until it gets ignited. The temperature was monitored using the thermometer. Time variation and temperature were noted during gel formation, fuming, ignition and combustion processes. Gel formed at ~150 °C and ignition started at ~170 °C. Reddish yellow combustion flame was appeared inside the beaker when the temperature reached about 190 °C. After completion of combustion above ~360 °C, the ash color powder was obtained. The final citrate combustion product was collected from the beaker, and subsequently annealed at 800, 900, 1000 and 1100 °C for 2 h in a in a groove rolled muffle furnace. After completion of annealing, the furnace was cooled to room temperature.

Materials characterization

The quality and phases of present samples were examined by means of powder X-ray diffraction (Bruker, D8 Advanced) method using Cu K_α radiation ($\lambda = 1.54156$ Å) at room temperature. The XRD raw data were analyzed with the JANA2006 software (Petricek et al. 2006), from which the cell parameters were calculated by the least-square method. The thermal decomposition of the combustion product was traced by thermal gravimetric and differential thermal analyses in air atmosphere from room temperature to 1000 °C in a thermal analysis system (TG/DTA6300 module EXSTAR series, Seiko Instruments Inc., Japan). The Fourier-transform infrared (FT–IR) spectra were recorded on a Perkin-Alpha optic instrument equipped with KBr beam splitter spectrometer at a resolution of 4 cm^{-1}. A very small amount of present series powder sample was mixed finely with little amount of KBr and pressed in a cylindrical (13 mm) die under three ton pressure to obtain a thin disk like pellet. The FT-IR spectra were recorded at ambient conditions in the wavelenumber range from 4000 to 400 cm^{-1}. The photoluminescence (PL) spectra of the annealed powder samples were performed in a spectrofluorometer (ELICO SL 174) using 150 Watt Xenon Arc lamp as the excitation light source. The near infrared (NIR) spectra of all the combustion product and annealed materials were performed in an NIR spectrophotometer (ELICO SL 153) using a quartz halogen lamp as the light source. The surface morphological images and the elements present in the selected $BaFe_{12}O_{19}$ powder sample were analyzed by the field emission scanning electron microscope; FESEM (F E IQuanta FEG 200) attached with energy dispersive X-ray analyzer. The magnetic hysteresis curve of the selected $BaFe_{12}O_{19}$ powder was measured by vibrating sample magnetometer (VSM) with a maximum applied field of 15 kOe at room temperature.

Results and discussion

Thermogravimetric analysis of citrate sol–gel combustion product

The combustion product obtained by citrate sol–gel method was studied by TG–DTA analysis and their respective TG and DTA curves are demonstrated in Fig. 1. The weight loss of ∼1.6 % is seen in the TG curve from the initiation up to ∼400 °C. This weight loss can be assigned for the liberation of the surface absorbed species of the as-prepared combustion product. Followed by about ∼2.8 % of weight loss is seen between ∼400 and ∼780 °C. This weight loss may be related to the removal of residual volatile species present in the combustion product. No significant weight loss (∼0.2 %) is observed between ∼780 and ∼850 °C. Further no weight loss is noticed in the TG curve above 900 °C, which is confirming the formation of main $BaFe_{12}O_{19}$ phase material. The weight losses seen in the TGA curve concur with endothermic thermal events seen in the DTA curve at ∼375, ∼500 and ∼850 °C. A small exothermic-like peak is observed at ∼850 °C in DTA curve is due to the phase formation temperature of $BaFe_{12}O_{19}$ materials (Vinod et al. 2011).

Powder XRD structural analysis

Figure 2a–e illustrates the powder XRD patterns of as-prepared citrate sol–gel combustion product, and subsequently annealed at different temperature powder samples. The XRD pattern of as-prepared (Fig. 2a) material clearly indicates that the expected $BaFe_{12}O_{19}$ phase was not formed in the combustion process. From the literature, we learnt that the formation of $BaFe_{12}O_{19}$ phase was found to involve two steps, that is the formation of $BaFe_2O_4$ phase, followed by the reaction between $BaFe_2O_4$ and iron oxide (α- or γ-Fe_2O_3) (Shang et al. 2007; Mali and Ataie 2004, 2005; Qiu and Gu 2006). According to Mali and Ataie (2005), the XRD pattern of their as-burnt powder indicates the presence of γ-Fe_2O_3 as a major phase and some other minor phases, namely α-Fe_2O_3, $BaCO_3$, BaO_2 and $BaFe_{12}O_{19}$. At first sight we can say that the XRD pattern of our citrate sol–gel combustion product implies the formation of cubic spinel phase. Therefore, we tried to identify the formation of cubic spinel phase for the possible nominal composition $BaFe_2O_4$ and Fe_3O_4 from the XRD pattern of combustion product, though $BaFe_2O_4$ is not reported as a cubic phase in literature. First, we tried to extract the lattice parameters for the composition, $BaFe_2O_4$ for a cubic structure using space group, Fd-3m (227) with formula unit, $Z = 8$, taking $MgFe_2O_4$ as standard cubic phase (Ohbayashi and Iida 1967). All the reflections of combustion product match for the cubic spinel phase (for example, $BaFe_2O_4$), except one strong impurity peak ($2\theta = 23.94°$). Using JANA 2006 software, the cubic lattice parameter, $a = 0.835(1)$ nm is obtained which is in good agreement with the cubic spinel phase (Ohbayashi and Iida 1967). While the $BaFe_2O_4$ phase is reported (Candeia et al. 2007; Pawar and Pardeshi 2014) as an orthorhombic spinel like space group, Bb21m (36) with lattice parameters, $a = 1.9042$ nm, $b = 0.53838$ nm and

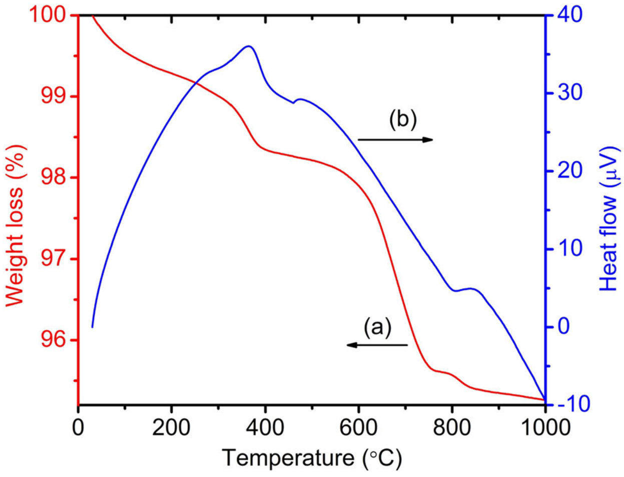

Fig. 1 Thermogram profiles of citrate sol–gel derived as-prepared material: TGA (*a*), and DTA (*b*)

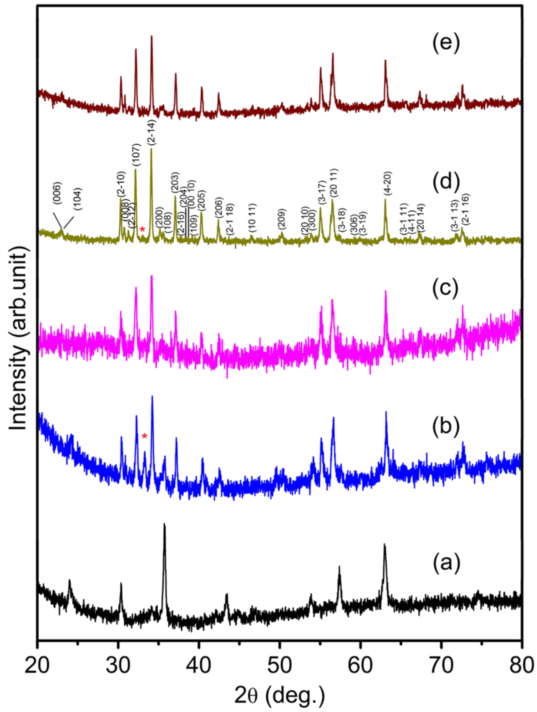

Fig. 2 XRD patterns of as-prepared (*a*) and annealed $BaFe_{12}O_{19}$ materials: 800 °C (*b*), 900 °C (*c*), 1000 °C (*d*), and 1100 °C (*e*). The symbol *asterisk* indicates the impurity of α-Fe_2O_3 phase

$c = 0.84445$ nm (JCPDS 46-0113), our citrate sol–gel combustion product material exhibits almost cubic spinel type $BaFe_2O_4$ phase (see, Fig. 3a). A strong peak seen at $2\theta = 23.94°$ in Fig. 2a is owing due to the presence of $BaCO_3$ phase (Pawar and Pardeshi 2014). Quite similar cubic spinel structure of $CoFe_2O_4$ phase was found in the literature for the cobalt substituted, $Ba_{1-x}Co_xFe_{12}O_{19}$ phase ($x = 1.0$) (Chavan et al. 2016). Further, we tried to find out the formation of cubic spinel Fe_3O_4 phase from the XRD pattern of combustion product which exhibits $a = 0.836(1)$ nm, is in good agreement with the cubic spinel (Fe_3O_4) phase (see, Fig. 3b). Therefore, we believe that our citrate sol–gel combustion product is crystallized mainly in cubic phase (with the nominal composition either $BaFe_2O_4$ or Fe_3O_4). But other possible phase cannot be completely ruled out as there is a signature for the growth of extra peaks ($2\theta = 34.11°$, $34.74°$ and $44.76°$) and its intensities are close to the background level. As we are

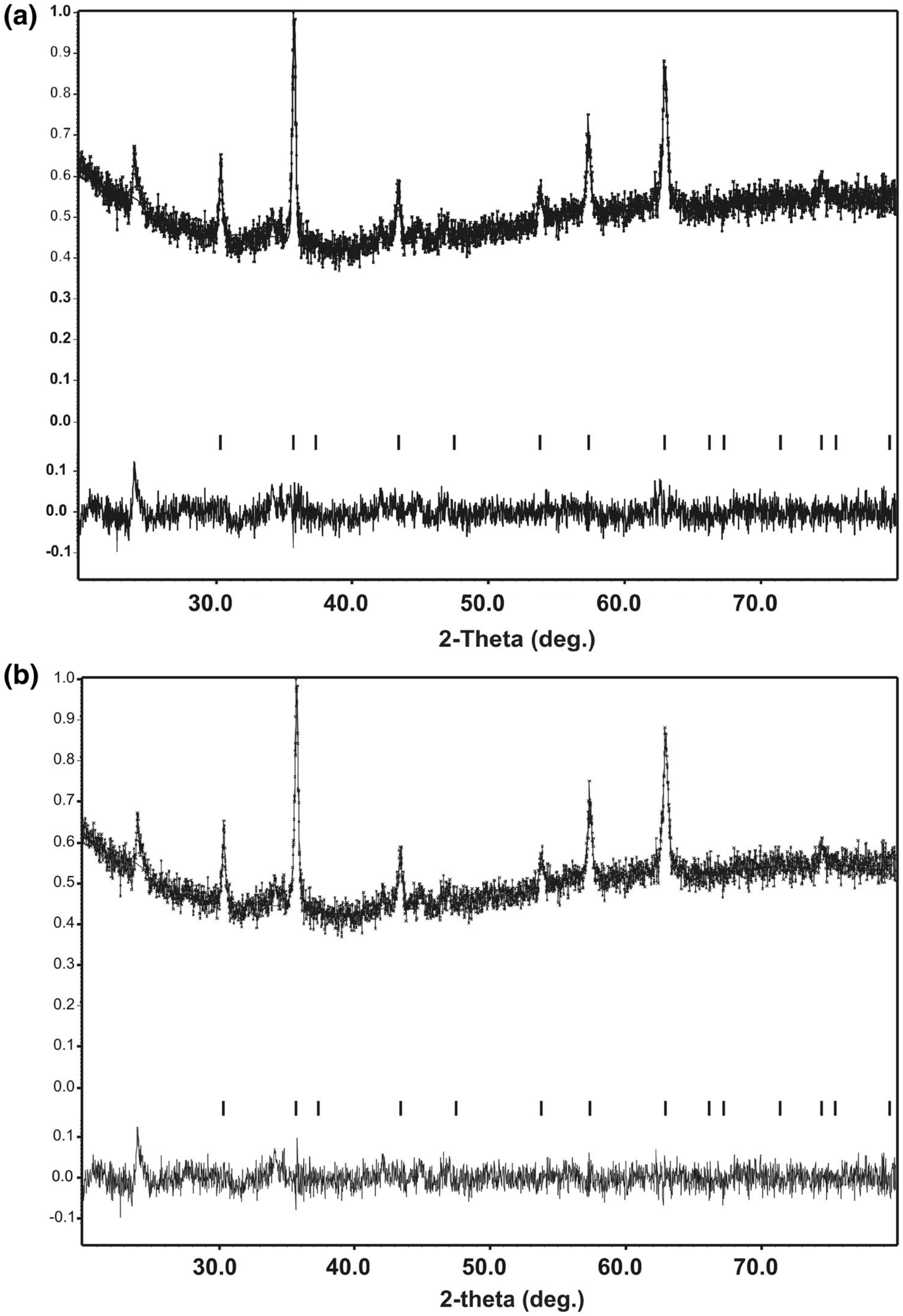

Fig. 3 XRD pattern of as-prepared combustion product refined for the cubic phase: $BaFe_2O_4$ (**a**) and Fe_3O_4 (**b**). *Solid lines at the bottom* are the difference between the observed and calculated patterns. *Vertical lines at the bottom* show the position of allowed Bragg peaks

interested in the main phase ($BaFe_{12}O_{19}$) materials, we believe that it is needless to stress much about the citrate sol–gel combustion product.

To obtain the $BaFe_{12}O_{19}$ phase, the citrate sol–gel combustion product was annealed at four different temperatures, such as 800, 900, 1000 and 1100 °C for 2 h. Interestingly, the annealing treatment enhanced the $BaFe_{12}O_{19}$ phase formation. The sample annealed at 800 °C exhibits a small peak at $2\theta = 33.1°$ due to α-Fe_2O_3 impurity phase in addition to the main $BaFe_{12}O_{19}$ phase. Upon increasing the annealing temperature, the impurity (α-Fe_2O_3) peak is almost disappeared and only the $BaFe_{12}O_{19}$ phase was present in the annealed powders. Further. the crystalline nature of $BaFe_{12}O_{19}$ phase is improved by annealing at 1000 and 1100 °C. The indexed peaks (Fig. 2d) are due to hexagonal $BaFe_{12}O_{19}$ phase (Balamurugan et al. 2015). High temperature annealing results the formation of phase pure $BaFe_{12}O_{19}$ materials, but it increases the crystallinity/crystalline size which is supposed less nanostructured. As the phase formation of nanostructured $BaFe_{12}O_{19}$ materials is rather complicated and sensitive to many parameters, it is rather difficult to predict the ideal annealing temperature of $BaFe_{12}O_{19}$ materials. However, from our present study we confirm that 1000 °C is the ideal annealing temperature for the formation of phase pure nanocrystalline $BaFe_{12}O_{19}$ materials. Further from the literature (Jiang et al. 2010; Balamurugan et al. 2015; Topal et al. 2007; Radwan et al. 2007; Mali and Ataie 2005) we learnt that many reports suggest 1000 °C is the ideal annealing temperature for the formation of phase pure $BaFe_{12}O_{19}$ materials. The structural parameters, such as lattice parameter, cell volume, density, average crystalline size, dislocation density, lattice strain, micro strain and stacking fault of the present series samples are extracted from the structural refinement using the XRD data. The crystalline size (D) was extracted by the Debye–Scherrer equation which is expressed as $D = K\lambda/\beta\cos\theta$, where $K = 0.9$, λ is the wavelength of X-ray radiation (Cu K_{α}) used for diffraction, β is the full width half maxima (FWHM), and θ is the diffraction angle. The average crystalline size (D) is found in the range of 32–42 nm for the annealed samples (see Table 1). The value of D increases with increase of annealing temperature. The dislocation density, lattice strain, micro strain, and stacking fault for the present series samples are extracted from $\delta = 1/D^2$ (Sathyamoorthy et al. 2006; Sharma et al. 2011; Touati et al. 2014; Bindu and Thomas 2014), $\varepsilon = \beta/4 \times \tan\theta$ (Thool et al. 2014), $\varepsilon = \beta \times \cos\theta/4$ (Sathyamoorthy et al. 2006; Sharma et al. 2011) and $SF = 2\pi^2/45\sqrt{(3\tan\theta)}$ (Touati et al. 2014; Thool et al. 2014), respectively, and their values are given in Table 1. From Table 1 we notice that the dislocation density, lattice strain, micro strain, and stacking fault for the annealed samples decrease with the increase of annealing temperature.

HRSEM micrographs and EDX quantitative analysis of $BaFe_{12}O_{19}$ nanomaterials

The surface morphology of the selected (annealed at 1000 °C) good quality nanocrystalline $BaFe_{12}O_{19}$ material was examined using HRSEM and EDX techniques. The different HRSEM images taken under different magnifications are presented in Fig. 4a–d. The lower magnification images (a, b) seem thin plate-like flakes morphology with random sizes with moderate agglomeration of nanoparticles. Under higher magnification, the micro images (c, d) also reveal the same features with the measured size of the range of 100–200 nm. Agglomeration seems unavoidable due to the magnetic interaction between the nanocrystalline $BaFe_{12}O_{19}$ particles (Jiang and Ai 2010; Sathyamoorthy et al. 2006). In some cases, the micro image crystalline/grain sizes of samples are larger than the crystalline size estimated by XRD (Ebrahimi et al. 2012; Balamurugan and Melba 2015). For example, the XRD crystalline size of present $BaFe_{12}O_{19}$ nanomaterials is found to be ~44 nm, whereas the HRSEM micrograph showed 100–200 nm. The inconsistency in crystalline sizes obtained from XRD and SEM/TEM is ascribed to the non-isometric shape of $BaFe_{12}O_{19}$ nanomaterials (Yu and Lin 2004) and polycrystalline nature of the materials (Ebrahimi et al. 2012; Balamurugan and Melba 2015). The wide range of XRD crystalline sizes of $BaFe_{12}O_{19}$ nanomaterials are reported as 95 nm (Murthy et al. 2012), 38.2–72.1 nm (Liu and Xiang 2010), 32.6–71.1 nm (Song et al. 2010), 44–53 nm (Ebrahimi et al. 2012), and 33 nm (Yu and Lin 2004) for the citrate sol–gel processed materials by different research groups. The literature survey on the morphological images we could see the wide range (30–500 nm and in somes ~6 μm) of particle/grain sizes for the citrate sol–gel processed $BaFe_{12}O_{19}$ materials. The particles in different shapes, namely spherical, polygonic, plate-like shape with random orientation, hexagonal, small elongated, polyhedrons with clear cut boundaries, hollow spherical, flaky are reported for the $BaFe_{12}O_{19}$ materials. Though agglomeration of nanoparticles appears unavoidable in most of the combustion derived nanocrystalline materials, it is possible to prevent the agglomeration by surface functionalization of the nano ferrites with various types of organic ligands for example polymers, proteins, pepetides and small organic molecules (Durmus et al. 2011; Jiang et al. 2010; Birsoza et al. 2010; Ting and Wu 2010). In the present citrate sol–gel synthesis, citric acid acts as fuel to complete the combustion reaction. By modifying the synthesis condition, the surface functionalization of nano hexa-ferrites with the organic ligands is possible to prevent

Table 1 Structural parameters, such as lattice parameters, volume, density, crystalline size, average crystalline size, dislocation density, lattice strain, micro strain and stacking fault of as-prepared and annealed $BaFe_{12}O_{19}$ materials

Annealing temperature (°C)	Lattice parameters		Volume (nm^3)	Density (g/cm^3)	Crystalline size[a] (nm)	Average crystalline size (nm)	Dislocation density $\times 10^{15}$ ($lines/m^2$)	Lattice strain $\times 10^{-3}$	Micro strain $\times 10^{-3}$ ($lines^{-2}/m^{-4}$)	Stacking fault
	a (nm)	*c* (nm)								
800	0.5887 (8)	2.321 (4)	0.696 (2)	5.30 (1)	35.84	32.06	1.07	2.9	1.11	0.3989
900	0.5888 (9)	2.320 (5)	0.696 (2)	5.30 (1)	34.068	31.97	1.00	2.85	1.09	0.3906
1000	0.5887 (3)	2.320 (1)	0.696 (8)	5.30 (6)	44.43	39.94	0.674	2.49	0.88	0.4118
1100	0.5891 (3)	2.321 (1)	0.697 (8)	5.30 (6)	44.38	41.81	0.581	2.27	0.83	0.4009

[a] Calculated from 2 to 14 reflection for the annealed samples

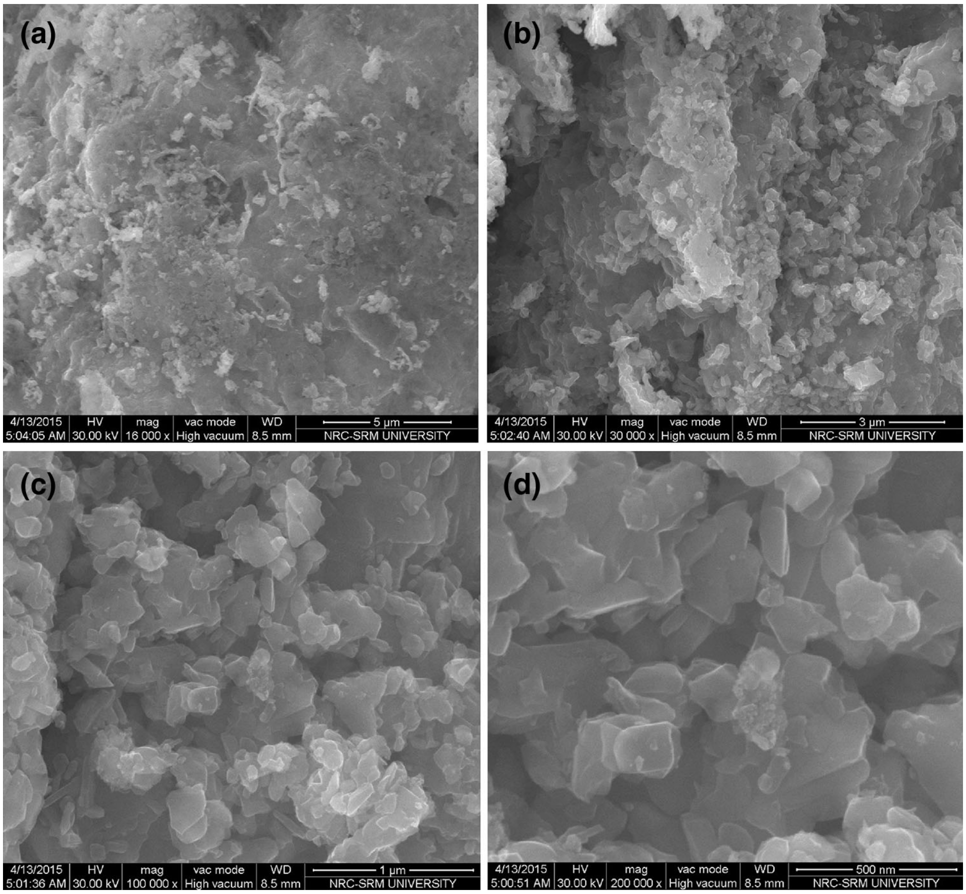

Fig. 4 HRSEM micro images of annealed $BaFe_{12}O_{19}$ materials taken under different magnifications: 16,000× with 5 μm par scale (**a**), 30,000× with 3 μm par scale (**b**), 100,000× with 1 μm par scale (**c**), and 200,000× with 500 nm par scale (**d**)

the agglomeration (Durmus et al. 2011; Jiang et al. 2010). However, this should be confirmed by conducting further experiments. The surface morphology of the hybrid hexaferrite materials should be evaluated by comparing of hexa ferrite material before and after the functionalization.

The energy dispersive X-ray (EDX) analysis was performed on the present surfaces of thin plate-like flakes materials to examine the presence of elemental composition and the EDX spectrum is displayed in Fig. 5. The EDX spectrum reveals the presence of Ba, Fe, and O elements in the $BaFe_{12}O_{19}$ materials at the correct proportion without any impurity phases. The extracted EDX quantitative data are given in the Table 2. The appearance of carbon (C) peak is owing to the carbon grid used as a sample holder.

FT-IR spectra of present series samples

Figure 6 exhibits the FT-IR spectra taken in the wavenumber range of 4000–400 cm^{-1} for the combustion

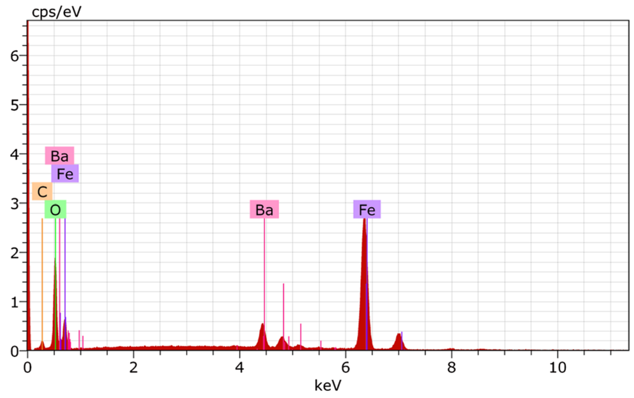

Fig. 5 EDX spectrum of annealed $BaFe_{12}O_{19}$ material

Table 2 Quantitative elemental analysis of annealed (1000 °C) nanocrystalline $BaFe_{12}O_{19}$ materials

Element	Atomic number	Series	Wt%	At.%
Ba	56	L	7.66	1.30
Fe	26	K	39.84	16.68
O	8	K	41.60	60.80
C	6	K	10.89	21.21
Total			100	100

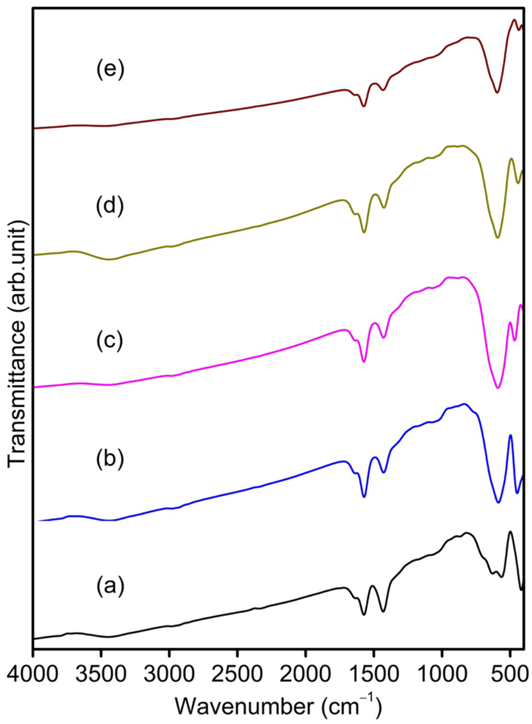

Fig. 6 FT-IR spectra of as-prepared (*a*) and annealed $BaFe_{12}O_{19}$ materials: 800 °C (*b*), 900 °C (*c*), 1000 °C (*d*), and 1100 °C (*e*)

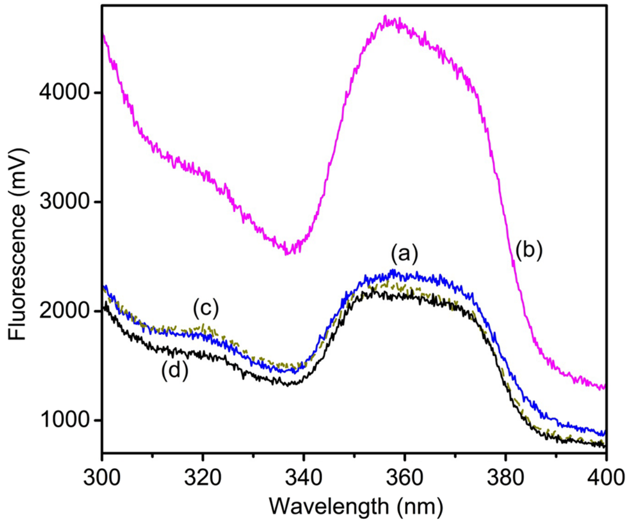

Fig. 7 PL emission spectra of different annealed $BaFe_{12}O_{19}$ materials: 800 °C (*a*), 900 °C (*b*), 1000 °C (*c*), and 1100 °C (*d*). The excitation wavelength, $\lambda^{ex} = 270$ nm

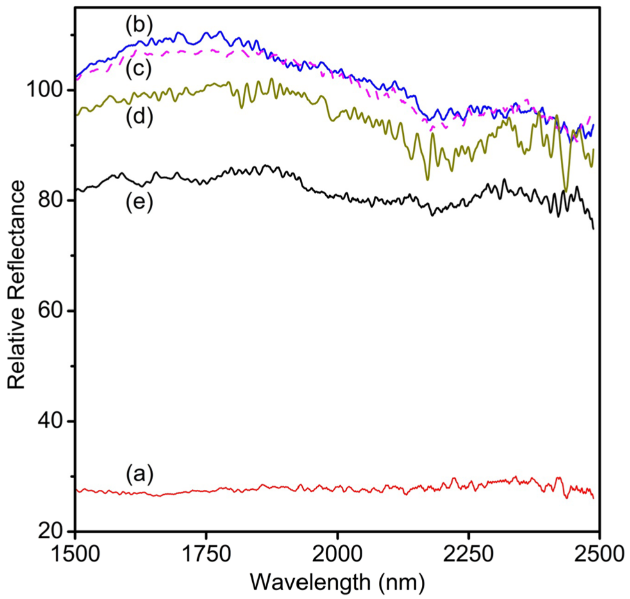

Fig. 8 NIR spectra of as-prepared (*a*) and annealed $BaFe_{12}O_{19}$ materials: 800 °C (*b*), 900 °C (*c*), 1000 °C (*d*), and 1100 °C (*e*)

product and annealed (800, 900, 1000, and 1100 °C) materials. The FT-IR spectra of all the present samples show two IR characteristics bands between 420 and 600 cm^{-1} which are attributed to the Fe–O stretching vibration of ferrite materials (Jiang et al. 2010; Parkin et al. 2001). Further few additional FT-IR bands are seen between 1000 and 4000 cm^{-1} in all the present samples due to the stretching vibrations of atmospheric species (H_2O/OH and CO_3^{2-}) adsorbed on the surface of the materials (Huang et al. 2003; Hong et al. 2004; Qiu et al.

2005). A minor broad IR bandseen at ~3480 cm^{-1} in all the samples is due to O–H stretching band of H_2O (Huang et al. 2003). The IR bands seen at ~1640 and ~1452 cm^{-1} for all samples can be indexed for the anti symmetrical and symmetrical stretching vibrations of carbonate species (Hong et al. 2004). The band lying from 1380 to 1400 cm^{-1} corresponds to the antisymmetrical and symmetrical stretching vibrations of COO^- (Huang et al. 2003).

PL emission spectra of $BaFe_{12}O_{19}$ materials

The room temperature PL emission spectra of different annealed (at different temperatures such as 800, 900, 1000, and 1100 °C) $BaFe_{12}O_{19}$ materials are presented in Fig. 7. The PL emission spectra are taken under the excitation wavelength, $\lambda^{ex} = 270$ nm for all annealed samples. The PL emission spectrum of $BaFe_{12}O_{19}$ material exhibits a broad emission peak at ~360 nm. Similar to the present $BaFe_{12}O_{19}$, the $BaFe_{12}O_{19}$ material prepared by co-precipitation method has also shown a PL emission peak at ~360 nm under excitation wavelengths of 270 nm (Balamurugan and Resmi 2015). The fluorescence intensity increases upon annealing the combustion product at 900 °C, and then decreases significantly with increasing annealing temperature to 1100 °C.

NIR spectra of $BaFe_{12}O_{19}$ materials

The NIR spectra measured in the spectral region, 1500–2500 nm for the combustion product as well as different annealed $BaFe_{12}O_{19}$ materials are shown in Fig. 8a–e.

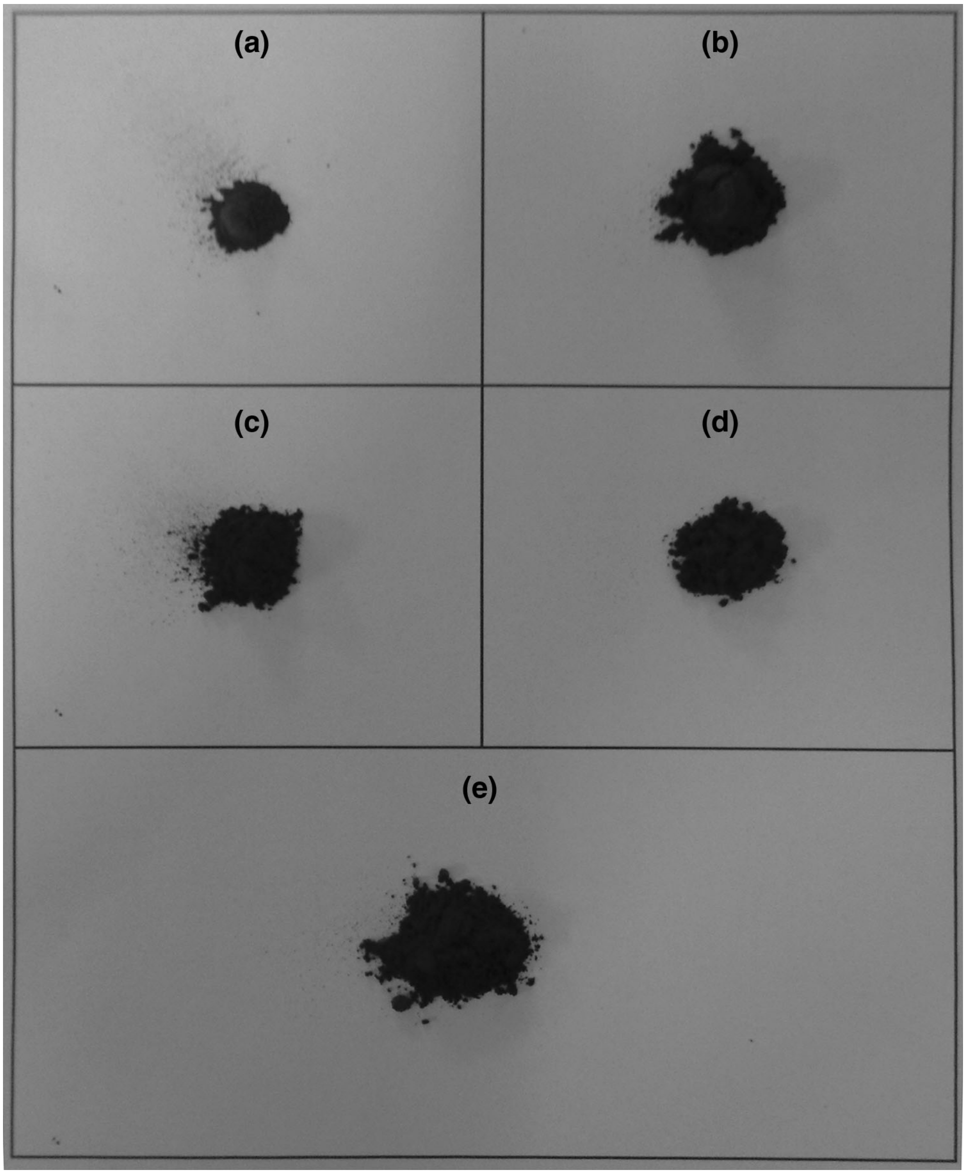

Fig. 9 Visual appearance (*color*) of present series samples: as-prepared (**a**) and annealed $BaFe_{12}O_{19}$ materials: 800 °C (**b**), 900 °C (**c**), 1000 °C (**d**), and 1100 °C (**e**)

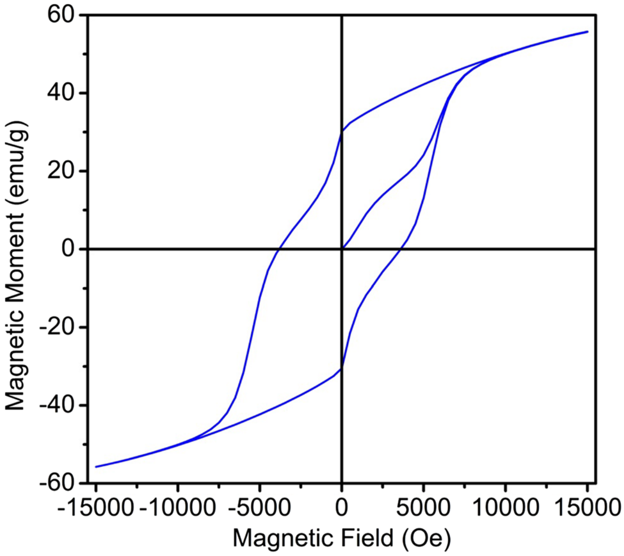

Fig. 10 Magnetic hysteresis loop of annealed $BaFe_{12}O_{19}$ sample recorded at room temperature

From this figure we notice that the annealed hexagonal $BaFe_{12}O_{19}$ phase materials reveal high (85–110 %) NIR relative reflectivity at ~1750 nm, whereas the combustion product shows ~28 % NIR relative reflectivity in the wavelength range, 1500–2500 nm. Among the different annealed samples, the $BaFe_{12}O_{19}$ material obtained after annealing at 800 °C shows higher (~110 %) NIR relative reflectance than other annealed samples. Though annealing yielded single phase of $BaFe_{12}O_{19}$, it suppressed the NIR reflectivity of the annealed materials which may be due to the increase in the crystalline size of the annealed samples. The visual appearance (dark brown color) of the present series samples are shown in Fig. 9a–e. From this we could see no significant variation in color of the present pigments. It is important to note that the NIR relative reflectivity of the nanocrystalline $BaFe_{12}O_{19}$ materials obtained by citrate sol–gel synthesis method is higher than the nanocrystalline $BaFe_{12}O_{19}$ materials obtained by mechano-thermal (Qiu et al. 2005) and co-precipitation method (Balamurugan and Resmi 2015). The present dark brown colored $BaFe_{12}O_{19}$ materials can be applied as ceramic color pigment which includes several applications.

Like the present hexa-ferrite, $BaFe_{12}O_{19}$ materials, there are several spinel ferrites and other ferrites are also found to use as NIR pigment (Candeia et al. 2007; Chaudhry et al. 2015; Benda and Kalendová 2013; Costa et al. 2008; Opuchovic et al. 2015; Liu et al. 2015). As the NIR pigment has found potential applications in solar reflective and color pigment, currently the research is focused to identify the different novel pigments. Our recent article summarizes the literature survey on the NIR reflectivity of some binary oxides and complex oxide systems (Balamurugan et al. 2016). Generally, binary oxides show high NIR reflectivity in the NIR region. However, some complex oxide systems (Balamurugan et al. 2016) also show high NIR reflectivity. Due to the impact of citrate sol–gel synthesis method, the present hexa-ferrite $BaFe_{12}O_{19}$ materials have also competent to binary oxides to show high NIR reflectivity.

Magnetic properties of nanocrystalline $BaFe_{12}O_{19}$ material

The magnetic hysteresis loop (M–H) for the selected (1000 °C) $BaFe_{12}O_{19}$ sample was recorded at room temperature with increasing magnetic fields up to ±15 kOe; $-15\ \mathrm{kOe} \leq H \leq 15\ \mathrm{kOe}$. The M–H curve is depicted in Fig. 10. The resultant magnetic values of the coercive field, (H_c), magnetization (M_s), and retentivity (M_r) are found to be 3705.3 Oe, 55.774, and 30.313 emu/g, respectively. These M_s, M_r, and H_c values are comparable to the literature values reported for the $BaFe_{12}O_{19}$ phase materials (Durmus et al. 2011; Jiang et al. 2010; Shang et al. 2007; Vinod et al. 2011; Mali and Ataie 2005; Birsoza et al. 2010; Xu et al. 2006; Sozeri et al. 2012; Jiang and Ai 2010; Mali and Ataie 2004; Qiu and Gu 2006; Parkin et al. 2001; Hong et al. 2004; Rafique et al. 2013; Castro et al. 1997; Ounnunkad and Winotai 2006). The ratio M_r/M_s of the present $BaFe_{12}O_{19}$ sample is found to be 0.543 which is comparable to the reported values (Shang et al. 2007; Birsoza et al. 2010). The wasp-waist-like shape of the hysteresis loop reveals that the major $BaFe_{12}O_{19}$ phase may contains trace amount of magnetic impurity (α- or γ-Fe_2O_3) phase that cannot be detected by the limit of XRD technique. Such a wasp-waist-like shape of the hysteresis loop was reported in the literature for the $BaFe_{12}O_{19}$ phase (Mali and Ataie 2005; Wang et al. 2007). Table 3 summarizes the room temperature magnetic properties of the hexagonal $BaFe_{12}O_{19}$ phase materials obtained by sol–gel combustion methods (Durmus et al. 2011; Jiang et al. 2010; Shang et al. 2007; Vinod et al. 2011; Mali and Ataie 2004, 2005; Birsoza et al. 2010; Xu et al. 2006; Sozeri et al. 2012; Jiang and Ai 2010; Qiu and Gu 2006; Parkin et al. 2001; Hong et al. 2004; Rafique et al. 2013; Castro et al. 1997; Ounnunkad and Winotai 2006). From this Table 3 we notice the important magnetic characteristics of $BaFe_{12}O_{19}$ and/or some doped $BaFe_{12}O_{19}$ phase materials.

Though the $BaFe_{12}O_{19}$ materials have been synthesized largely by citrate sol–gel method and characterized by various techniques, to our knowledge the optical studies based on NIR reflectivity and photoluminescence characterizations have not been reported for the citrate sol–gel synthesized $BaFe_{12}O_{19}$ materials. Thus, we believe that the NIR reflectivity and photoluminescence characterizations presented here for the citrate sol–gel synthesized $BaFe_{12}O_{19}$ materials is the novelty of this work. Further, the TG/

Table 3 Literature survey on magnetic properties of $BaFe_{12}O_{19}$ materials obtained by sol–gel combustion method

Applied magnetic field	Saturation magnetization (M_s)	Remanence (M_r)	Coercive field (H_c)	Magnetic features of $BaFe_{12}O_{19}$ materials	References
At room temperature up to 15 kOe	–	–	–	Hysteresis curves do not saturate at high fields, which is a characteristic feature of fine particle systems with grain sizes smaller than 1 µm	Durmus et al. (2011)
15 kOe	61.4 emu/g	–	–	–	Jiang et al. (2010)
12,000 Oe	53 emu/g	–	5.3 kOe	–	Shang et al. (2007)
9 kOe	40.443 emu/g	22.287 emu/g	5689.28 Oe	–	Vinod et al. (2011)
–	61.2 A m^2/kg		405.9 kA/m	The best magnetic properties and micro-structural characteristics are obtained for the sample calcined at 1000 C for 1 h	Mali and Ataie (2005)
At room temperature (25 °C) 15 kOe	67 emu/g and it is close to the theoretical value of 72 emu/g	–	4.5 kOe	The ratio of M_r/M_s for the bulk $BaFe_{12}O_{19}$ powders (bulk refers to the without coating) is around 0.55 which indicates that particles are within the single domain limit (i.e., <1 µm)	Birsoza et al. (2010)
3T at room temperature	60.13 emu/g	–	432 kA/m	Magnetic properties decreased when pH > 10. It is believed that higher pH (>10) does not adapt to produce well-crystalline powder	Xu et al. (2006)
–	Varies from 52.4 to 62.3 emu/g with increasing temperature	–	4287 Oe	The maximum magnetization obtained is rather far from the theoretical value of 72 emu/g reported for $BaFe_{12}O_{19}$	Sozeri et al. (2012)
15 kOe	47 emu/g	–	700 Oe	Exhibiting the characteristics of hard magnetic materials.	Jiang and Ai (2010)
20 kOe	49.76 emu/g	26.50 emu/g	4861 Oe	The well-shaped $BaFe_{12}O_{19}$ grains obtained at relatively low temperatures can improve the magnetic properties of the ferrite	Mali and Ataie (2004)
–	56.0, 56.2, 57.0, and 57.3 Am^2/kg respectively for the milling time of 0, 10, 20 and 60 h	–	350.14, 421.76, 421.76, and 425.74 kA/m respectively, according with the milling time of 0, 10, 20, and 60 h	The saturation magnetization is not obviously affected by the variation of the powder size. The great variation of the powder size results in the increasing coercivity	Qiu and Gu (2006)
–	35.10 emu/g	–	2660 Oe	–	Parkin et al. (2001)
–	62.0 emu/g	30.4 emu/g	2850 Oe	–	Hong et al. (2004)
–	57.8 emu/g	–	5285 Oe	The main magnetic characteristics should be due to the high purity (1 % of impurities), the good crystalline state, and the small homogeneous size of the particles	Castro et al. (1997)
–	–	–	2–5 kOe	The increase in coercivity is due to finer grains	Ounnunkad and Winotai (2006)

DTA thermograms (Fig. 1) of our citrate sol–gel synthesized combustion product are rather different from the literature reports (Durmus et al. 2011; Vinod et al. 2011; Mali and Ataie 2004, 2005; Song et al. 2010) as it shows the plausible formation of cubic phase which is confirmed by XRD analysis (Fig. 3).

Conclusion

The present citrate sol–gel synthesis method yielded good quality hexagonal phase $BaFe_{12}O_{19}$ nanomaterials upon annealing the as-prepared combustion product at 800–1000 °C for 2 h. The powder XRD, TG, FT-IR, HRSEM-EDX, NIR, PL, magnetization, and UV-visible absorption techniques were used for the characterization of the present work. From the XRD results, we noticed that the phase transformation of cubic spinel phase of the combustion product to hexagonal $BaFe_{12}O_{19}$ phase for the annealed materials. Thin plate-like flakes morphology with random sizes of around 100–200 nm particles are seen in the $BaFe_{12}O_{19}$ materials. The present $BaFe_{12}O_{19}$ nanomaterial has potential application in NIR reflective color pigment as this citrate sol–gel method has significantly enhanced the NIR reflectivity of the annealed materials. The field depend magnetization of the annealed $BaFe_{12}O_{19}$ sample exhibited a M_s of 55.774 emu/g under the extreme applied magnetic field of 15 kOe.

Acknowledgments The author S. Balamurugan is thankful to Tamilnadu State Council for Science and Technology (TNSCST) (Ref.: AR/PS/2012–2013/209) for the partial support to the present work. The Pondicherry University, Central Instrumentation Facility (CIF) is acknowledged for extending the analytical service in the form of VSM measurement. The HRSEM-EDX for the present sample was performed at the nanotechnology research centre of SRM University, India is also acknowledged.

References

Balamurugan S, Melba K (2015) $Zn_{1-x}Cu_xO$ ($0.02 \le x \le 0.1$) nanomaterials prepared by ball milling, citrate sol–gel, and molten salt flux methods. J Nanosci Nanotechnol 15:4632–4640

Balamurugan S, Resmi SP (2015) Synthesis of nanocrystalline $BaFe_{12}O_{19}$ materials by co-precipitation method using KOH and K_2CO_3 as precipitating agent. Adv Sci Eng Med 7:183–189

Balamurugan S, Brightlin BC, Kiruba VSA (2015) Synthesis of $BaFe_{12}O_{19}$ materials by mechano-thermal route: novel inorganic pigment with high near-infrared reflectance. J Nanosci Nanotechnol 15:9494–9499

Balamurugan S, Dheebikha K, Gokul Raja TS (2016) Nanocrystalline $Gd_2Ti_2O_7$ pyrochlore material for NIR reflective pigment application: micro-structural and optical studies. J Nanosci Nanotechnol 16:677–688

Benda P, Kalendová A (2013) Anticorrosion properties of pigments based on ferrite coated zinc particles. Phys Proced 44:185–194

Bindu P, Thomas S (2014) Estimation of lattice strain in ZnO nanoparticles: X-ray peak profile analysis. J Theor Appl Phys 8:123–134

Birsoza B, Baykala A, Sozerib H, Toprakc MS (2010) Synthesis and characterization of polypyrrole–$BaFe_{12}O_{19}$ nanocomposite. J Alloys Compd 493:481–485

Candeia RA, Souza MAF, Bernardi MIB, Maestrelli SC, Santos IMG, Souza AG, Longo E (2007) Monoferrite $BaFe_2O_4$ applied as ceramic pigment. Ceram Int 33:521–525

Castro S, Gayoso M, Rodroguez C (1997) A study of the combustion method to prepare fine ferrite particles. J Solid State Chem 134:227–231

Chaudhry Ali U, Mittal Vikas, Mishra Brajendra (2015) Nano nickel ferrite ($NiFe_2O_4$) as anti-corrosion pigment for API 5L X-80 steel: an electrochemical study in acidic and saline media. Dyes Pigm 118:18–26

Chavan VC, Shirsath SE, Mane ML, Kadam RH, More SS (2016) Transformation of hexagonal to mixed spinel crystal structure and magnetic properties of Co^{2+} substituted $BaFe_{12}O_{19}$. J Magn Magn Mater 398:32–37

Chen W, Zheng J, Li Y (2012) Synthesis and electromagnetic characteristics of $BaFe_{12}O_{19}$/ZnO composite material. J Alloys Compd 513:420–424

Costa ACFM, Leite AMD, Ferreira HS, Kiminami RHGA, Cava S, Gama L (2008) Brown pigment of the nanopowder spinel ferrite prepared by combustion reaction. J Eur Ceram Soc 28:2033–2037

Durmus Z, Unal B, Toprak MS, Sozeri H, Baykal A (2011) Synthesis and characterization of poly(3-thiophenyl acetic acid) (P3TAA)–$BaFe_{12}O_{19}$ nanocomposite. Polyhedron 30:1349–1359

Ebrahimi Y, Alvani AAS, Sarabi AA, Sameie H, Salimi R, Alvani MS, Moosakhani S (2012) A comprehensive study on the magnetic properties of nanocrystalline $SrCo_{0.2}Fe_{11.8}O_{19}$ ceramics synthesized via diverse routes. Ceram Int 38:3885–3892

Hong YS, Ho CM, Hsu HY, Liu CT (2004) Synthesis of nanocrystalline $Ba(MnTi)_xFe_{12-x}O_{19}$ powders by the sol–gel combustion method in citrate acid–metal nitrates system ($x = 0$, 0.5, 1.0, 1.5, 2.0). J Magn Magn Mater 279:401–410

Huang J, Zhuang H, Li WL (2003) Synthesis and characterization of nano crystalline $BaFe_{12}O_{19}$ powders by low temperature combustion. Mater Res Bull 38:149–159

Jiang J, Ai LH (2010) Facile synthesis, characterization and properties of Ba-hexaferrite/ZnO hybrid structures. Phys B 405:2640–2642

Jiang J, Ai LH, Liu L-Y (2010) Poly(aniline-co-o-toluidine)/$BaFe_{12}O_{19}$ composite: preparation and characterization. Mater Lett 64:888–890

Liu M, Xiang J (2010) Formation and characterization of magnetic barium ferrite hollow fibers with high specific surface area via sol-gel process. Solid State Sci 12:1603–1607

Liu L, Han A, Ye M, Feng W (2015) The evaluation of thermal performance of cool coatings colored with high near-infrared reflective nano-brown inorganic pigments: magnesium doped $ZnFe_2O_4$ compounds. Sol Energy 113:48–56

Mali A, Ataie A (2004) Influence of the metal nitrates to citric acid molar ratio on the combustion process and phase constitution of barium hexaferrite particles prepared by sol–gel combustion method. Ceram Int 30:1979–1983

Mali A, Ataie A (2005a) Structural characterization of nanocrystalline $BaFe_{12}O_{19}$ powders synthesized by sol–gel combustion route. Scripta Mater 53:1065–1070

Mali A, Ataie A (2005b) Influence of Fe/Ba molar ratio on the characteristics of Ba-hexaferrite particles prepared by sol–gel combustion method. J Alloys Compd 399:245–250

Murthy JK, Mitra C, Ramc S, Venimadhav A (2012) Temperature dependent magnetic and dielectric properties of M-type hexagonal B a$Fe_{12}O_{19}$ nanoparticles. J Alloys Compd 545:225–230

Ohbayashi K, Iida S (1967) Oxygen content and thermomagnetic properties in $Cu_{1-x}Mg_xFe_2O_4$. J Phys Soc Jpn 23:776–785

Opuchovic Olga, Kreiza Gediminas, Senvaitiene Jurate, Kazlauskas Karolis, Beganskiene Aldona, Kareiva Aivaras (2015) Sol-gel synthesis, characterization and application of selected submicrosized lanthanide (Ce, Pr, Nd, Tb) ferrites. Dyes Pigment 118:176–182

Ounnunkad S, Winotai P (2006) Properties of Cr-substituted M-type barium ferrites prepared by nitrate–citrate gel-autocombustion process. J Magn Magn Mater 301:292–300

Parkin IP, Elwin G, Kuznetsov MV, Pankhurst QA, Bui QT, Forster GD, Barquin LF, Komarov AV, Morozov YG (2001) Self-propagating high temperature synthesis of $MFe_{12}O_{19}$ M = (Sr, Ba) from the reactions of metal superoxides and iron metal. J Mater Proc Technol 110:239–243

Pawar RY, Pardeshi SK (2014) Selective oxidation of styrene to benzaldehyde using soft $BaFe_2O_4$ synthesized by citrate gel combustion method. Arab J Chem. doi:10.1016/j.arabjc.2014.08.012

Petricek V, Dusek M, Palatinus L (2006) Jana 2006. The crystallographic computing system. Institute of Physics, Praha

Ping JW, Ying L, Lin ZM, Jie QY, Tian X (2008) Comparison of the sol-gel method with the coprecipitation technique for preparation of hexagonal barium ferrite. Chem Res Chin Univ 24(5):525–528

Qiu J, Gu M (2006) Crystal structure and magnetic properties of barium ferrite synthesized using GSPC and HEBM. J Alloys Compd 415:209–212

Qiu J, Haigen S, Gu M (2005a) Microwave absorption of nanosized barium ferrite particles prepared using high-energy ball milling. Powder Technol 154:116–119

Qiu J, Liang L, Gu M (2005b) Nanocrystalline structure and magnetic properties of barium ferrite particles prepared via glycine as a fuel. Mater Sci Eng, A 393:361–365

Radwan M, Rashad MM, Hessien MM (2007) Synthesis and characterization of barium hexaferrite nanoparticles. J Mater Proc Technol 181:106–109

Rafique MS, Anjum S, Siraj K (2013) Magnetic anisotropy in nanocrystalline $BaFe_{12}O_{19}$ thin films deposited under various applied magnetic fields. Thin Sol Film 545:608–613

Sathyamoorthy R, Chandramohan S, Sudhagar P, Kanjilal D, Kabiraj D, Asokan K (2006) Structural and photoluminescence properties of swift heavy ion irradiated CdS thin films. Sol Energy Mater Sol Cel 90:2297–2304

Shang H, Wang J, Liu Q (2007) Synthesis and characterization of nanocrystalline $BaFe_{12}O_{19}$ obtained by using glucose as a fuel. Mater Sci Eng, A 456:130–132

Sharma G, Gosavi SW, Lochab SP, Singh N (2011) Effect of swift heavy ion irradiation on Ce doped CaS nanophosphors. AIP conference proceedings 1391, 558. doi:10.1063/1.3643609

Song F, Shen X, Xiang J, Zhu Y (2010) Characterization and magnetic properties of $Ba_xSr_{1-x}Fe_{12}O_{19}$ ($x = 0$–1) ferrite hollow fibers via gel-precursor transformation process. J Alloys Compd 507:297–301

Sozeri H, Durmus Z, Baykal A, Uysal E (2012) Preparation of high quality, single domain $BaFe_{12}O_{19}$ particles by the citrate sol–gel combustion route with an initial Fe/Ba molar ratio of 4. Mater Sci Eng, B 177:949–955

Thool GS, Singh AK, Singh RS, Gupta A, Susan MABH (2014) Facile synthesis of flat crystal ZnO thin films by solution growth method: a micro-structural investigation. J Saudi Chem Soc 18:712–721

Ting T-H, Wu K-H (2010) Synthesis, characterization of polyaniline/$BaFe_{12}O_{19}$ composites with microwave-absorbing properties. J Magn Magn Mater 322:2160–2166

Topal U, Ozkan H, Dorosinskii L (2007) Finding optimal Fe/Ba ratio to obtain single phase $BaFe_{12}O_{19}$ prepared by ammonium nitrate melt technique. J Alloys Compd 428:17–21

Touati R, Rabeh MB, Kanzari M (2014) Structural and optical properties of the new absorber Cu_2ZnSnS_4 thin films grown by vacuum evaporation method. Energy Proced 44:44–51

Vinod ND, Mane ML, Babrekar MK, Kale CM, Jadhav KM (2011) Influence of chromium substitution on structural and magnetic properties of $BaFe_{12}O_{19}$ powder prepared by sol–gel auto combustion method. J Alloys Compd 509:4394–4398

Wang J, Chen Q, Che S (2004) Magnetic properties in $BaFe_{12}O_{19}$ nanoparticles prepared under a magnetic field. J Magn Magn Mater 280:281–286

Wang J, Wu Y, Zhu Y, Wang P (2007) Formation of rod-shaped $BaFe_{12}O_{19}$ nanoparticles with well magnetic properties. Mater Lett 61:1522–1525

Xu G, Ma H, Zhong M, Zhou J, Yue Y, He Z (2006) Influence of pH on characteristics of $BaFe_{12}O_{19}$ powder prepared by sol–gel auto-combustion. J Magn Magn Mater 301:383–388

Xu P, Han X, Zhao H, Liang Z, Wang J (2008) Effect of stoichiometry on the phase formation and magnetic properties of $BaFe_{12}O_{19}$ nanoparticles by reverse micelle technique. Mater Lett 62:1305–1308

Yu H-F, Huang K-C (2003) Effects of pH and citric acid contents on characteristics of ester-derived $BaFe_{12}O_{19}$ powder. J Magn Magn Mater 260:455–461

Yu H-F, Lin H-Y (2004) Preparation and thermal behavior of aerosol-derived $BaFe_{12}O_{19}$ nanoparticles. J Magn Magn Mater 283:190–198

Yu H-F, Liu P-C (2006) Effects of pH and calcination temperatures on the formation of citrate-derived hexagonal barium ferrite particles. J Alloys Compd 416:222–227